RSC Advances

PAPER

Cite this: *RSC Adv.*, 2023, **13**, 16248

A novel n–p heterojunction $Bi_2S_3/ZnCo_2O_4$ photocatalyst for boosting visible-light-driven photocatalytic performance toward indigo carmine†

Nguyen Thi Mai Tho, *[a] Nguyen Van Cuong,[a] Viet Ha Luu Thi, [a] Nguyen Quoc Thang [a] and Phuc Huu Dang*[b]

Received 28th April 2023
Accepted 25th May 2023

DOI: 10.1039/d3ra02803h

rsc.li/rsc-advances

An innovative p–n heterojunction $Bi_2S_3/ZnCo_2O_4$ composite was first fabricated *via* a two-step co-precipitation and hydrothermal method. By controlling the weight amount of Na_2S and $Bi(NO_3)_3$ precursor, different heterogeneous $xBi_2S_3/ZnCo_2O_4$ were synthesized (x = 0, 2, 6, 12, and 20). The p–n heterojunction $Bi_2S_3/ZnCo_2O_4$ was characterized by structural, optical, and photochemical properties and the photocatalyst decoloration of indigo carmine. Mott–Schottky plots proved a heterojunction formed between n-Bi_2S_3 and p-$ZnCo_2O_4$. Furthermore, the investigation of the photocurrent response indicated that the $Bi_2S_3/ZnCo_2O_4$ composite displayed an enhanced response, which was respectively 4.6 and 7.3 times (4.76 μA cm^{-2}) greater than that of the pure Bi_2S_3 (1.02 μA cm^{-2}) and $ZnCo_2O_4$ (0.65 μA cm^{-2}). Especially the optimized p–n $Bi_2S_3/ZnCo_2O_4$ heterojunction with 12 wt% Bi_2S_3 showed the highest photocatalyst efficacy of 92.1% at 40 mg L^{-1} solutions, a loading of 1.0 g L^{-1}, and a pH of 6 within 90 min of visible light illumination. These studies prove that p–n $Bi_2S_3/ZnCo_2O_4$ heterojunction photocatalysts can greatly boost their photocatalytic performance because the inner electric field enhances the process of separating photogenerated electron–hole pairs. Furthermore, this composite catalyst showed good stability and recyclability for environmental remediation.

1. Introduction

Currently, environmental pollution in the world is at an alarming level, especially water pollution. Wastewater including pigments, reactive dyes, heavy metal ions, and organic substances is the main cause of pollution because it is difficult to decompose and highly resistant to light, heat, and oxidizing agents that can affect the health of humans and organisms.[1,2] A typical indigo dye used in textile dyeing and other industries is indigo carmine ($C16_6H_8N_2Na_2O_8S_2$). However, indigo carmine (IC) is a very dangerous agent that is categorized as being environmentally toxic; regular exposure to it can irritate the respiratory tract, the skin on the back of the eyes, and the cornea, in addition to causing acute toxicity. Therefore, the pollution control and treatment of IC dyes from textile dyeing wastewater are of great interest to many people.[3–5] Over the past few years, advanced oxidation processes (AOPs) provide a possibility for completing the cleaning of wastewater polluted with recalcitrant organic chemicals.[6] A number of these methodologies are frequently employed in Advanced Oxidation Processes (AOPs), including (i) Fenton oxidations, (ii) photocatalysts, (iii) plasma oxidation, and (iv) ozonation. Recently, metal oxide semiconductor photocatalysis has been widely explored. WO_3, TiO_2, ZnO, Fe_2O_3, ZrO_2, CuO, and NiO are semiconductor photocatalysts.[7] However, these metal oxide semiconductors only take advantage of the UV radiation spectrum (3–5% of the total solar spectrum) because of their wide bandgap.[8] Moreover, hybrid metal chalcogenide compounds can have adequate redox potential while improving solar spectrum absorption.[9–11] Among the hybrid metal chalcogenide compounds, n-type bismuth sulfide (Bi_2S_3), possesses unique properties such as wide light absorption, high dielectric properties, a narrow band gap (E_g) (approx. 1.3 eV), lamellar structure, and especially an adjustable band gap, so it is used in photocatalysis and photo electrochemistry (PEC).[12–16] Unfortunately, the photogenerated electron–hole pair ($e_{CB}^- - h_{VB}^+$) recombines rapidly due to the narrow E_g of Bi_2S_3, resulting in low separation efficiency and challenging its reality-based applications.[6] So, scientists look for solutions such as dopants, decoration with the plasmonic noble metal, novel (p–n/n–n) heterojunction formation, *etc.*[17–21]

[a]*Faculty of Chemical Engineering, Industrial University of Ho Chi Minh City, Ho Chi Minh, Vietnam. E-mail: nguyenthimaitho@iuh.edu.vn*

[b]*Faculty of Fundamental Science, Industrial University of Ho Chi Minh City, Ho Chi Minh, Vietnam. E-mail: danghuuphuc@iuh.edu.vn*

† Electronic supplementary information (ESI) available. See DOI: https://doi.org/10.1039/d3ra02803h

Recent research has focused on the transition metal p-type oxide $ZnCo_2O_4$ due to its narrow energy band, higher photoelectrochemical stabilization, higher electrical conductivity, and a larger amount of redox reaction sites than metal oxides (ZnO, Co_3O_4).[22,23] It is noted that because of the specific energy band structure, the valence band (VB) is formed by the energy levels of O 2p, while the conduction band is formed by the energies of Co 3d. So, the electron inside the band gap can switch easily, thus increasing the photogenerated electron–hole lifetimes.[24] Besides, $ZnCo_2O_4$ is a promising candidate for fabricating an advanced p–n heterojunction in conjunction with other photocatalysts.[25] Some heterojunction structure was studied such as $SnO_2/ZnCo_2O_4$,[26] $ZnCo_2O_4/Bi_2O_3$,[25] $ZnO/ZnCo_2O_4$,[27] $CaFe_2O_4/ZnCo_2O_4$,[28] $BiVO_4/ZnCo_2O_4$ in the photodegradation of dye molecules from aqueous solution.

Based on the above discussion, p–n heterojunctions structure including an n-type narrow bandgap Bi_2S_3 was deposited on the surface of p-type $ZnCo_2O_4$, which is the solution to boost the photocatalyst efficacy of $ZnCo_2O_4$. The structure with 12 wt% Bi_2S_3 on $ZnCo_2O_4$ showed an improvement in visible light photocatalytic performance than that of pure Bi_2S_3 and $ZnCo_2O_4$. This is because $ZnCo_2O_4$ provides superior photoelectrochemical stability, whereas the low energy bandgap Bi_2S_3 boosts solar light absorption ability. The type-II heterojunction forms a built-in electric field between the interface of Bi_2S_3 and $ZnCo_2O_4$ semiconductors, which accelerates the separation of photocarriers and is good for applications related to energy harvesting. The process of degradation was thoroughly studied.

2. Experimental

2.1 Synthesis of $ZnCo_2O_4$

The $ZnCo_2O_4$ materials were fabricated by the coprecipitation method. A solution of 100 mL $Zn(NO_3)_2$ 0.1 M and 100 mL $Co(NO_3)_2$ 0.3 M with a Zn^{2+}/Co^{2+} molar ratio of 1/3 was slowly added to 50 mL of 1 M NaOH with a rate of 10 mL min^{-1}. The solution was unchanged at pH 10 using NaOH and was stirred. The after-precipitation solution was aged at 105 °C for 15 hours. The resulting powders were filtered, cleaned with de-ionized water numerous times, and heated at 100 °C for 10 hours. The black powder was thermally treated at 600 °C for 4 h to receive $ZnCo_2O_4$ (ZC).

2.2 Synthesis of Bi_2S_3

The sample Bi_2S_3 was formed by slowly adding 10 mL Na_2S dissolved in ethylene glycol (EG) to 50 mL EG containing $Bi(NO_3)_3$, with a molar ratio of Bi^{3+}/S^{2-} at 2/3. The Bi_2S_3 was collected, centrifuged, cleaned, and air-dried at 105 °C.

2.3 Synthesis of $Bi_2S_3/ZnCo_2O_4$ heterostructures

First, the as-prepared 0.5 g $ZnCo_2O_4$ and $Bi(NO_3)_3 \cdot 5H_2O$ which were diluted in a minimum amount of HNO_3 (5%) before being dispersed, were inserted into 50 mL of EG. The solution of 50 mL Na_2S with EG was added dropwise and slowly to the as-prepared solution. The suspension solution was stirred at 140 °C for 12 hours. Eventually, the Bi_2S_3/ZC samples were gathered following deionized water washing and 100 °C drying. By controlling the weight amounts of Na_2S and $Bi(NO_3)_3$, different $Bi_2S_3/ZnCo_2O_4$ heterogeneous were obtained (x is the mass percentage of $Bi_2S_3/ZnCo_2O_4$). Four samples are labeled as $2.0Bi_2S_3$/ZC; $6.0Bi_2S_3$/ZC; $12.0Bi_2S_3$/ZC and $20.0Bi_2S_3$/ZC.

The obtained Bi_2S_3, ZC, and $x.0Bi_2S_3$/ZC powder were identified by X-ray diffraction (XRD), Fourier-transform infrared spectroscopy (FT-IR) microscopy (TEM), scanning electron microscopy (SEM), and X-ray photoelectron spectroscopy (XPS); the UV-visible diffuse reflectance spectrum (DRS); the energy dispersive X-ray (EDX), high-resolution electron microscope image (HRTEM), BET data including N_2 adsorption–desorption isotherms, inductively coupled plasma optical emission spectroscopy (ICP-OES), photocurrent response (j–t) and electrochemical impedance spectra (EIS). The ion Zn and Co leaching was detected by ICP-OES.

2.4 Evaluating photocatalytic performance

The catalytic activity of $x.0Bi_2S_3$/ZC powder was evaluated based on the decomposition of IC dye ($\lambda_{max} = 612$ nm) using a 300 W halogen lamp (Osram, Germany). The catalytic reaction is carried out on a catalytic system consisting of two processes:

Adsorption processes: The adsorption–desorption equilibrium of indigo carmine on the surface of $x.0Bi_2S_3$/ZC catalysts was in the dark for 1 hour.

Degradation processes: The light source is turned on to perform the photocatalytic reaction for 90 min. After every 15 minutes, 5 mL of suspension is placed in the centrifuge system to remove the catalyst. The solution was stirred using a magnetic stirrer and circulating water to keep the room temperature. The ultraviolet-visible spectrophotometer determines the concentration of the IC solution.

3. Results and discussion

3.1 Characterization

The structure of the prepared catalyst is studied based on XRD spectroscopy (Fig. 1a). The strong and sharp diffraction peaks of ZC at 31.85°; 36.17°; 47,38°, 56.76°, 62.77°, and 67.67° ascribed with (220); (311); (400); (422); (511) and (440) lattice planes of homogeneous cubic spinel phase $ZnCo_2O_4$ (JCPDS no. 23-1390), proving that the ZC was successfully synthesized by coprecipitation method. The diffraction peaks of pure Bi_2S_3 at 2θ values 22.46; 25.12; 28.35, 31.71; 39.8; 45.3; 46.5; 58.7 coincide with the orthorhombic Bi_2S_3 phase (JCPDS no. 17-0320).[29] The XRD patterns of $x.0Bi_2S_3$/ZC heterostructures ($x = 2, 6$) are similar to those of ZC and do not appear to have diffraction peaks of pure Bi_2S_3. This can be caused by the low loading weight of Bi_2S_3 on ZC. However, $x.0Bi_2S_3$/ZC ($x = 12, 20$) heterostructures appear as main diffraction peaks of Bi_2S_3 the intensities of them increase according to the content percentage of Bi_2S_3 on heterostructures increasing. The above results suggest that the $x.0Bi_2S_3$/ZC heterostructures were successfully synthesized with good crystallinity and less impurity.

The FTIR spectra of Bi_2S_3, ZC, and $x.0Bi_2S_3$/ZC heterostructure are presented in Fig. 1b. The Bi_2S_3 sample exhibited

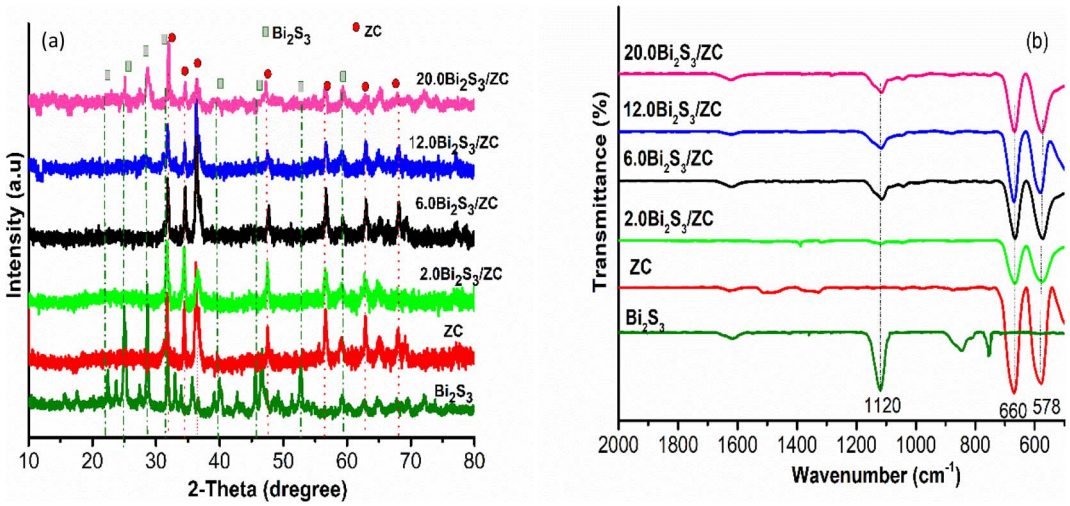

Fig. 1 XRD (a), FTIR (b) patterns for the Bi_2S_3, ZC, and $x.0Bi_2S_3$/ZC ($x = 2, 6, 12, 20$).

characteristic vibrational peaks at 1120 cm^{-1} relating to the stretching modes Bi–S groups.[30] For $x.0Bi_2S_3$/ZC samples characteristic bands of the stretching modes Bi–S are also observed at 1120 cm^{-1} and this indicates the presence of Bi_2S_3 in the composites. This peak was observed with lower intensities in the composites which indicates the formation of $x.0Bi_2S_3$/ZC heterojunction nanocomposites. In addition, the characteristic peaks of the ZC and $x.0Bi_2S_3$/ZC ($x = 2, 6, 12, 20$) are observed in 660 cm^{-1} and the range of 578 cm^{-1} which are metal-oxy vibration such as the Co–O tensile and the Zn–O spinel.[31]

In Fig. 2a, the synthesized Bi_2S_3 was clearly shown to produce nanoparticles with a homogeneous array, and porous material. Bi_2S_3 nanoparticles aggregated loosely, and there were apparent pores, indicating that adding additional active sites might boost catalytic activity. Many ZC layers were stacked resulting in typical nanoplates with a homogeneous array with thin sheets. FESEM image of $x.0Bi_2S_3$/ZC shows that Bi_2S_3 are precipitated and wrapped on the surface of ZC. Nanoparticles of Bi_2S_3 were coated on a surface of ZC, forming a heterogeneous interface with intimate contact. The more Bi_2S_3 content, the better $x.0Bi_2S_3$/ZC nanosheets become rough and irregular gradually.

In addition, the HRTEM results also confirmed the formation of the $12.0Bi_2S_3$/ZC heterojunction. The lattice fringes were approximately ~0.310 nm which is ascribed to the (221) plane of orthorhombic Bi_2S_3,[32,33] in which 0.239 nm belongs to the (311) plane of cubic spinel ZC.[23,28] In addition, the TEM image also observed the appearance of an amorphous phase at the interface of the crystalline Bi_2S_3 and ZC phases. The association

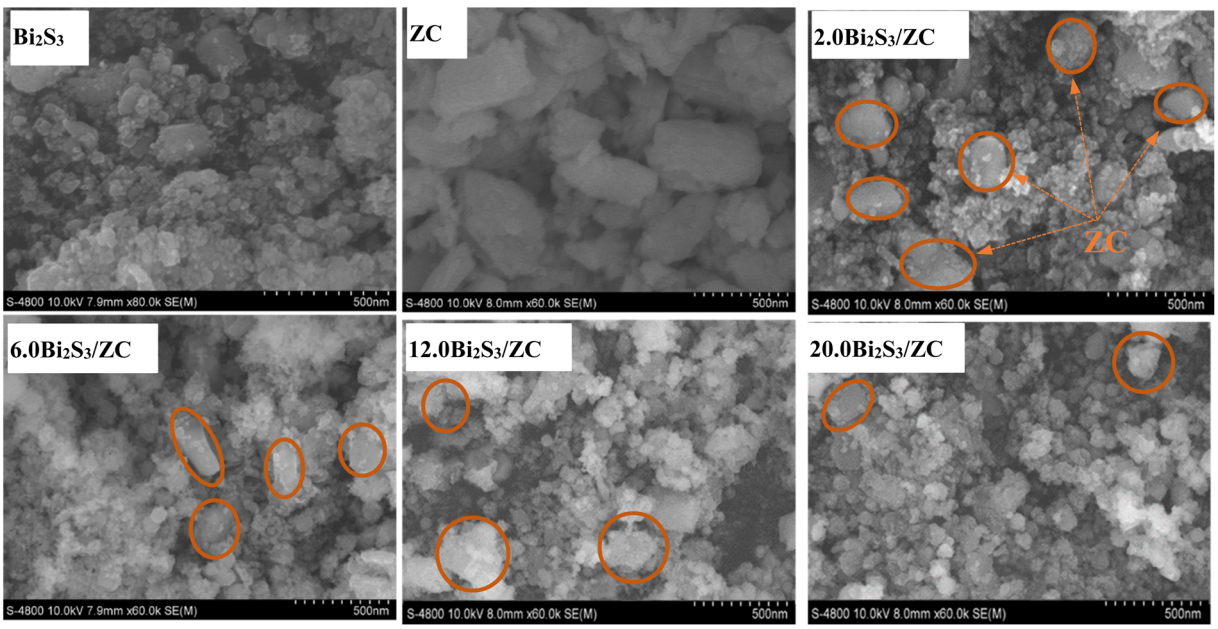

Fig. 2 The FESEM images of Bi_2S_3, $ZnCo_2O_4$ and $x.0Bi_2S_3$/ZC ($x = 2, 6, 12, 20$).

between the crystalline and amorphous phases helps speed up the charge migration due to the mobility of localization sites in the amorphous phase.[34] The distribution of particles was around 20-60 nm, which was determined by the TEM image (Fig. S1†). Moreover, Fig. 3c and d displays that the EDX spectra of ZC consists of only three main elements Zn (19.04%), Co (23.01%), O (57.94%) while the 12.0Bi_2S_3/ZC heterojunction shows the presence of Zn (28.93%), Co (7.18%), O (57.59%), Bi (1.47%) and S (4.82%). This result proved the formation of the Bi_2S_3/ZC heterojunction. Furthermore, the Co/Zn atomic ratio in ZC and 12.0Bi_2S_3/ZC are about 2.17 and 2.3 by ICP-OES measurement, respectively (Table S1†).

The optical absorption of Bi_2S_3, ZC, and x.0Bi_2S_3/ZC are shown in Fig. 4b. ZC shows good absorbance of light located at about 500 nm while pure Bi_2S_3 presents an optical absorption edge nearly in the visible light spectral region that extended even

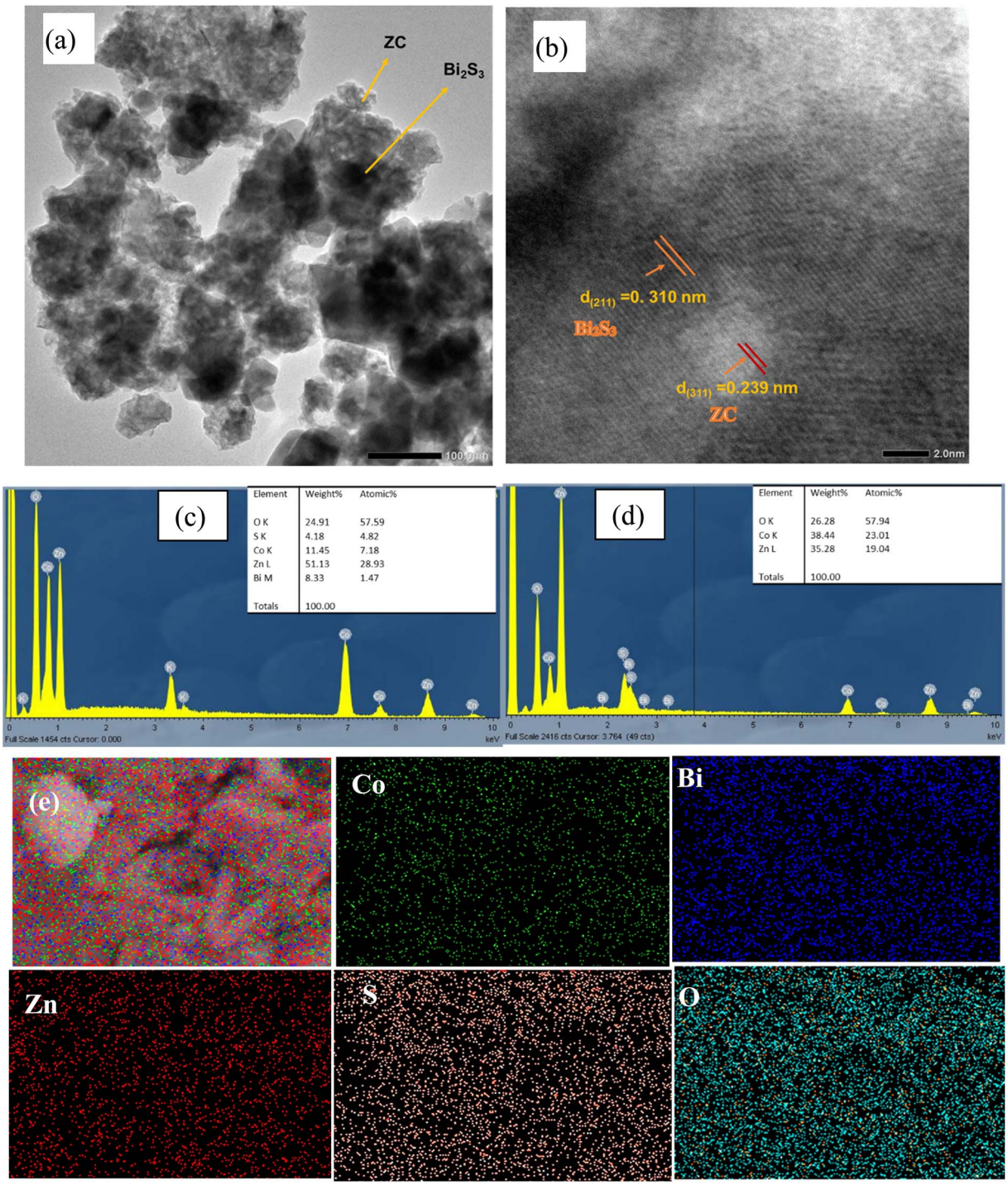

Fig. 3 TEM (a) and HRTEM (b) diagram of 12.0Bi_2S_3/ZC samples; the EDX (c–e) of $ZnCo_2O_4$ and 12.0Bi_2S_3/ZC samples.

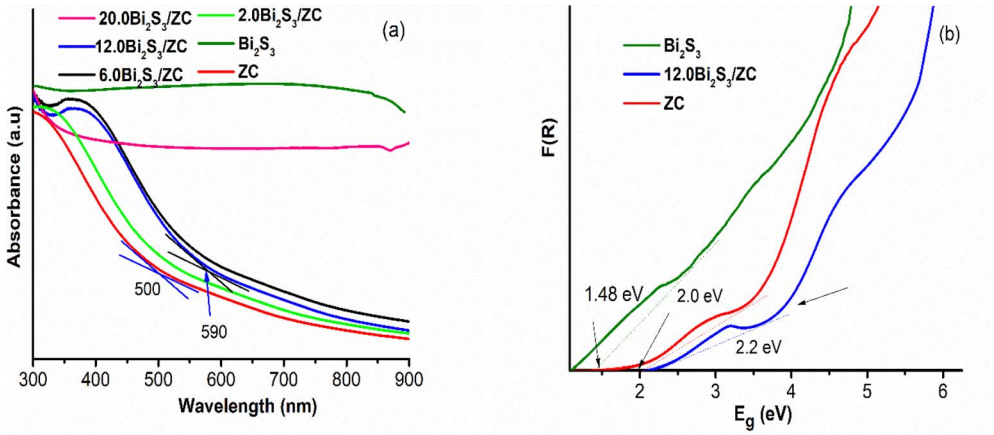

Fig. 4 (a) UV-vis DRS spectra, (b) band gap energies of ZC and Bi_2S_3.

to the infrared region. For the x.0Bi_2S_3/ZC heterojunction, the absorption edges have changed compared to ZC, edges appeared at 590 nm and were blue-shifted in comparison with those of ZC. It has been discovered that the proportion of the amount of Bi_2S_3 causes a change in the absorption edge and absorbance density in the visible spectrum. However, the band gap of 20.0Bi_2S_3/ZC will be dominated by the narrower band gap of Bi_2S_3 because Bi_2S_3 covers the surface of ZC. This phenomenon was observed in the morphology image FESEM. Besides, Using the Kubelka–Munk function estimate the band gap energy of the powders. Results can be seen from Fig. 4b that the bandgap of ZC, Bi_2S_3, and 12.0Bi_2S_3/ZC are approximately 2.2 eV, 1.48 eV, and 2.0 eV, respectively. The development of Bi_2S_3 nanoparticles on the surface of ZC can interface in heterojunction which increases more photogenerated hole–electron pair, thereby enhancing the photocatalytic performance of 12.0Bi_2S_3/ZC.[26,27]

The elements and chemical states in photocatalyst heterojunction were studied by X-ray photoelectron spectroscopy (XPS). As depicted in Fig. 5a Zn, Co, O, and S elements of both $ZnCo_2O_4$ and x.0Bi_2S_3/ZC were detected from characteristic peaks of O 1s; Co 2p and Zn 2p; x.0Bi_2S_3/ZC samples also have characteristic peaks of S 2p and Bi 4f.[22] The high-resolution spectrum for the S 2p and Bi 4f region shows (Fig. 5b) the number of deconvoluted peaks at 158.16 and 163.71 eV ascribed to Bi $4f_{7/2}$ and Bi $4f_{5/2}$ orbital, meanwhile, the peak at 161.22 eV and 162.64 eV can be ascribed to S $2p_{3/2}$ and S $2p_{1/2}$.[32,35] The first group at 779.37; 794.47 eV and the second group at 780.61; 795.88 eV binding energy (Fig. 5c) which can be ascribed to Co 2p in ZC indicating that the valence of Co^{3+} and Co^{2+} of ZC spinel, these peaks move to the direction of large binding energy with 780.53; 796.55 eV and 783.12; 802.14 eV in 12.0Bi_2S_3/ZC, respectively.[36] Moreover, a multivalent in ZC was observed by the two weaks satellite peaks, as mentioned in the literature. Fig. 5d shows the peaks of ZC are Zn $2p_{3/2}$ (1021.38 eV) and Zn $2p_{1/2}$ (1044.45 eV), respectively. Moreover, the existence of Zn^{2+} in the ZC structure was identified by the distance between two peaks $Zn2p_{3/2}$ and $Zn2p_{5/2}$ (23.07 eV). Besides, the shift of Zn2p orbitals peaks to the higher binding energies for the 12.0Bi_2S_3/ZC heterojunction, compared to ZC. The deconvolution O 1 s peak (Fig. 5e) using the Gaussian-based included 530.48 and 532.65 components, which were attributed to metal–oxygen bonds (O_2^-), the surface hydroxyl groups, and the O–H species absorbed water on the surface of ZC.[37] The positive shift of binding energy of O 1s for 12.0Bi_2S_3/ZC heterojunction compared to ZC indicates a change of the electron density, establishing an effective charge transfer between ZC and Bi_2S_3. This could be explained due to the interaction effect of the strong chemical bond between ZC and Bi_2S_3 changing the outer electron cloud densities of Co.[22,25,36] Finally, from the XPS results, we can conclude the 12.0Bi_2S_3/ZC photocatalyst contains the elements Bi, S, O, Co, and Zn, indicating that Bi_2S_3 was synthesized successfully and loaded on the surface of spinel phase $ZnCo_2O_4$ nanoparticles.

Fig. 6 shows the result of the N_2 adsorption/desorption isotherm and pore-size distribution of ZC and 12.0Bi_2S_3/ZC that all samples exhibited a type IV isotherm, and the hysteresis loops were the type of H3. The specific surface area, pore volume, and average pore size of the ZC and 12.0Bi_2S_3/ZC were shown in Table 1. The Specific surface area calculated from the Brunauer–Emmett–Teller (BET) isotherms is 15.49 $m^2\ g^{-1}$ and 21.33 $m^2\ g^{-1}$ for ZC and 12.0Bi_2S/ZC, respectively. The increased surface area of 12.0Bi_2S/ZC could be attributed to the loading of pores Bi_2S_3 nanoparticles. The pore size distribution of ZC is approximately 13.07 nm, while that of 12.0Bi_2S/ZC is 15.76 nm. The significant specific surface area and pore constructed help increase active sites, enhance organic dye adsorption, and effectively transfer charge carriers, thus enhancing the photocatalytic activity of 12.0Bi_2S_3/ZC.

3.2 Photoelectrochemical performance

The photoelectrochemical operation of the x.0Bi_2S_3/ZC in 0.5 M Na_2SO_4 solution was investigated to determine the separation and charge transfer efficiency. The photoelectrochemical efficiency of Bi_2S_3, ZC, and 12.0Bi_2S_3/ZC is shown in Fig. 7. Transient photocurrent response was tested in all samples (On and off interval time being 10 s). According to the transient photoelectric response (I–t curve) in Fig. 6a, the 10%-Bi_2S_3/ZC composite has a greater photocurrent intensity (4.76 μA cm^{-2})

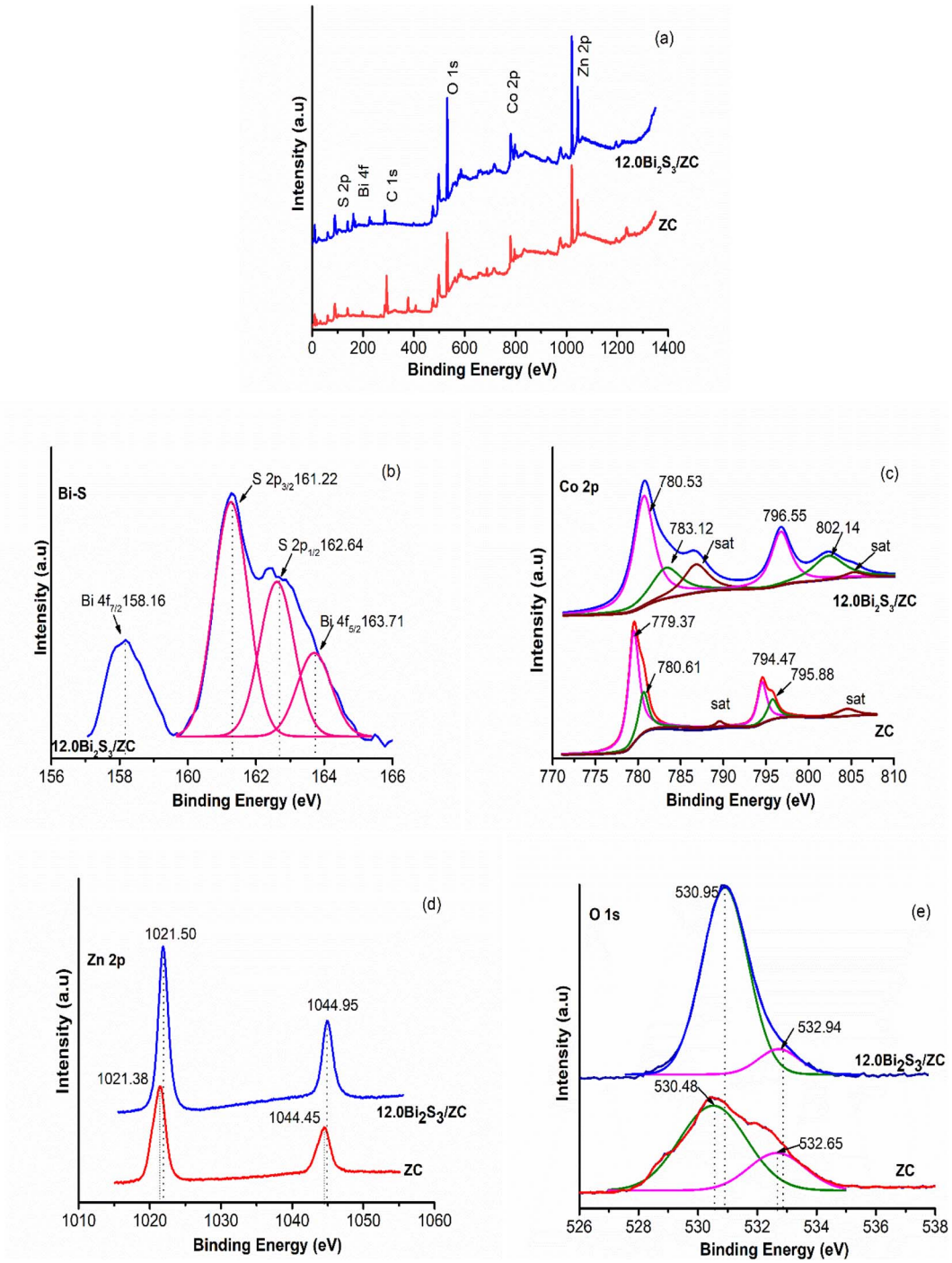

Fig. 5 XPS spectra (a) survey; (b) Bi–S 2p; (c) Co 2p; (d) Zn 2p; (e) O 1s of pristine $ZnCo_2O_4$ and 12.0Bi_2S_3/ZC samples.

than the pure Bi_2S_3 (1.02 μA cm^{-2}) and ZC (0.65 μA cm^{-2}). It is generally agreed that the separation of photogenerated charges is more effective, and its photocatalytic performance is the greater intensity of photocurrent.[35,38,39] Moreover, when the lamp is switched on, the photocurrent of 12.0Bi_2S_3/ZC continually rises, showing that the photogenerated electron–hole pairs separate continuously.

Electrochemical impedance spectroscopy (EIS) experiments correlate the charge transport resistance of a catalyst with the Nyquist plot, where a significant shift in the arc radius of the Nyquist plot indicates effective charge transport in the preparation of Bi_2S_3 – ZC. EIS of synthesized catalysts is displayed in Fig. 7b, and the equivalent circuit is shown in the upper right corner of Fig. 7b. Pure Bi_2S_3, ZC, and 12.0Bi_2S_3/ZC samples all have Rs values of 2627, 3012, and 1794 Ω, whereas the corresponding R_{ct} values are 43.34, 53.84, and 42.04 Ω. There is less resistance to charge transfer and more efficient carrier transfer when the semicircle's radius is smaller.[40,41] It can be observed

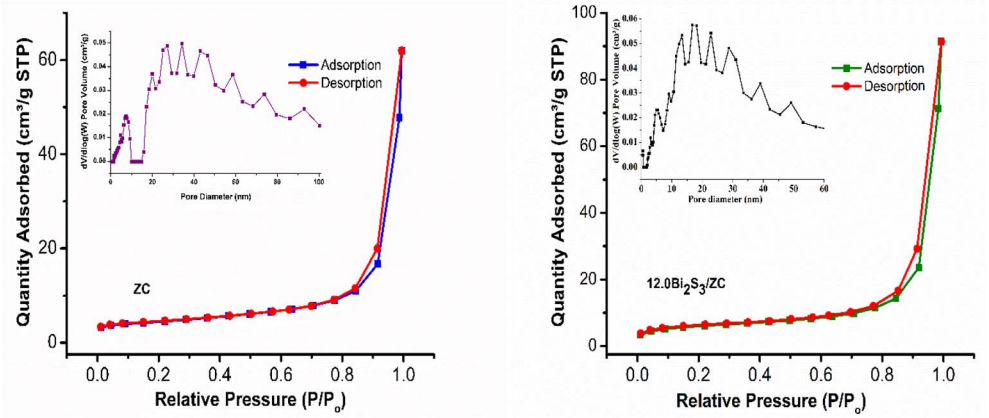

Fig. 6 Nitrogen adsorption–desorption isotherm and Barrett–Joyner–Halenda (BJH) pore-size distribution (a) ZC and 12.0Bi_2S_3/ZC.

Table 1 The specific surface area, pore volume, and average pore size of the ZC and 12.0Bi_2S_3/ZC

Sample	S_{BET} ($m^2\ g^{-1}$)	Pore volume ($cm^3\ g^{-1}$)	Average pore size (nm)
ZC	15.49	0.03566	13.07
12.0Bi_2S_3/ZC	21.33	0.04342	15.76

from the specific resistance values that the 12.0Bi_2S_3/ZC has the lowest resistance value, is more photo-catalytically active, and outperforms pure Bi_2S_3 and $ZnCo_2O_4$ in terms of surface charge transfer abilities. The EIS finding agreed with those from the UV-DRS characterization research and photocatalytic measurements.

The semiconductor and energy-gap structure of the photocatalyst was analyzed using the Mott–Schottky (M–S) measurement at 1000 Hz in 0.5 M Na_2SO_4 solution at pH 7. The acquired curve for $ZnCo_2O_4$ has a negative slope, suggesting that it is an n-type semiconductor, whereas the obtained curve for Bi_2S_3 has a positive slope, showing that it is a p-type semiconductor (see Fig. 7c). This study reveals that the CB potential of Bi_2S_3 and the VB potential of $ZnCo_2O_4$ are identified at −0.355 V *vs.* NHE and 1.535 V *vs.* NHE ($E_{NHE} = E_{Ag/AgCl\text{-}3.5M} + 0.24$), respectively. With the aforementioned results, it has been determined that the VB of Bi_2S_3 and CB of $ZnCo_2O_4$ are approximately 1.125 V and −0.665 V, respectively, as calculated by the formula $E_{CB} = E_{VB} - E_g$. To understand the mechanism of photocatalysis in the Bi_2S_3/$ZnCo_2O_4$ heterojunction, an M–S plot has been measured. The results indicate a flat band potential shift positive for the Bi_2S_3/$ZnCo_2O_4$ heterostructure photocatalyst, suggesting the formation of a p-ZC/n-Bi_2S_3 heterojunction. This finding is supported by previous research.[1,42]

3.3 Photocatalytic activity

3.3.1 Effect of a percentage of Bi_2S_3 in Bi_2S_3/ZC heterojunction. Fig. 8a and b displays the results of evaluating the photocatalytic activity of x.0Bi_2S_3/ZC catalysts (x = 2, 6, 12, 20) on the IC degradation process.

After a 60 minutes absorption process, the quantity of IC dye adsorbed from 29–33% for the adsorption equilibrium while after 90 minutes under the degradation process, the amount of IC degraded from 67% to 92.1% by x.0Bi_2S_3/ZC. The x.0Bi_2S_3/ZC heterostructures exhibit significantly increased photocatalytic performance as compared with ZC. The photodegradation efficiency of IC reached 92.1% for 12.0Bi_2S_3/ZC and only 53.8% for ZC. The photocatalytic experimental results of x.0Bi_2S_3/ZC obey the pseudo-first-order kinetic as indicated by the good values of the correlation coefficient (R^2 > 0.9588). The photocatalyst performance was determined by the values of k, which were subsequently arranged in descending order of 12.0Bi_2S_3/ZC (0.0230 min^{-1}) > 6.0Bi_2S_3/ZC (0.0158 min^{-1}) > 2.0Bi_2S_3/ZC (0.0126 min^{-1}) > 20.0Bi_2S_3/ZC (0.00828 min^{-1}) > ZC (0.00499 min^{-1}) > Bi_2S_3 (0.0042 min^{-1}).

The photocatalytic activity of x.0Bi_2S_3/ZC heterostructures was affected by Bi_2S_3 content. The photocatalytic activity of x.0Bi_2S_3/ZC heterostructures first increased and then decreased with increasing Bi_2S_3 content. The interaction between Bi_2S_3 and ZC boosts that improve the efficiency of charge separation, because of the contribution of the internal electric field between the junction surface between Bi_2S_3 and ZC. However, for the 20.0Bi_2S_3/ZC sample, the catalytic efficiency decreased markedly because the amount of Bi_2S_3 completely covered the ZC surface, leading to the loss of the number of light photons in the visible light region. This agrees with the UV-Vis DRS spectra and FESEM image.[26]

The amount of 0.5–2.0 g L^{-1} 12.0Bi_2S_3/ZC influence on photocatalytic degradation of IC was studied with unchanged the concentration of IC at 40 mg L^{-1} at pH 6.0 (Fig. 8c). When the loading of 12.0Bi_2S_3/ZC was changed from 0.5 to 1.0 g L^{-1}, the rate constant k of IC degradation increased significantly from 0.0068 to 0.0230 min^{-1}. However, the degradation efficiency decreases from 77.4% (k = 0.0121 min^{-1}) to 72% (k = 0.0067 min^{-1}) with catalyst loading of 1.5–2.0 g L^{-1}. The above results can be explained as follows: the overall amount of photon absorption and activity centers on the surface of the catalyst increases with increasing the catalyst loading. However, the catalyst loading considerably increases, and the increased

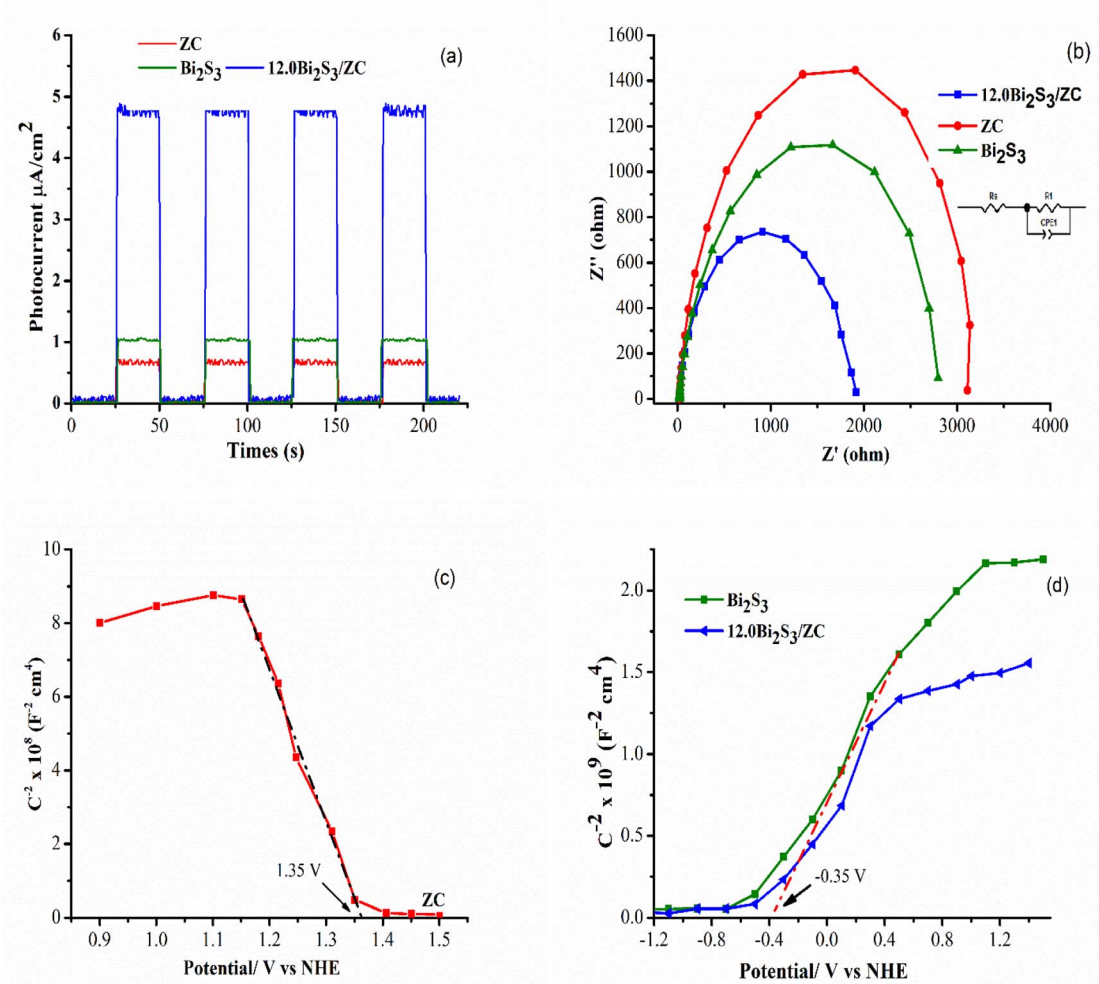

Fig. 7 (a) Transient photocurrent response; (b) EIS curves, (c and d) Mott–Schottky plot of ZC, 12.0Bi_2S_3, and 12.0Bi_2S_3/ZC.

turbidity prevented light transmission into the solution, thereby decreasing the activity of the catalyst.[43,44]

3.3.2 Effect of initial IC concentration. The photocatalytic activity of 12.0Bi_2S_3/ZC powder (1.0 g L^{-1}) was studied with various initial IC concentrations (20 to 50 mg L^{-1}) at pH 6 (Fig. 8d). The results showed that as the initial IC concentration changed from 20 to 50 mg L^{-1}, the degradation rate reduced from 0.661 to 0.162 min^{-1}. This reduces the number of photo-generated photons by obstructing the passage of light into the solution and onto the catalyst surface. As a result, there are fewer OH radicals formed on the surface, which reduces the process of IC decomposition.[43]

3.3.3 Effect of initial pH value. The degradation process of 40 mg L^{-1} IC of 1.0 g L^{-1} catalyst12.0Bi_2S_3/ZC was studied in pH ranges 4; 6; 8 (Fig. 9a). Following 90 minutes of visible light, the percentages and rate constant k of IC degradation at pH 4.0, 6.0, and 8.0 were 78.5% ($k = 0.0138$ min^{-1}), 92.1% ($k = 0.0230$ min^{-1}), 61.3% ($k = 0.0076$ min^{-1}), respectively, shown in Fig. 9. As pH_{pzc} 6.4 of 12.0Bi_2S_3/ZC > pH 4, and pH 6 of the solution, the surface of the catalyst gets positively charge. Consequently, electrostatic attraction between the negative charge of IC dye in solution and the positively charged 12.0Bi_2S_3/ZC catalyst surface leads to the increase of photocatalytic degradation. However, the degradation efficiency of IC at pH 4 is lower than that at pH 6 due to the large concentration of H^+, which hinders the attractive interaction between anion IC^- and the 12.0Bi_2S_3/ZC catalyst surface. While pH_{pzc} < pH 8, the electrostatic repulsion between the anionic IC solution and the negatively charged catalyst surface appears, thereby restricting the decomposition of the IC.[7,45]

3.3.4 Stability and reusability. The photochemical stability of 12.0Bi_2S_3/ZC (Fig. 9b) was tested with the initial IC concentration of 30 mg L^{-1}, pH 6.4, and the loading catalyst of 1.0 g L^{-1} under the presence of visible light. The used catalyst was centrifuged into distinct components before being cleaned with deionized water and heated at 110 °C. The IC dye degradation efficiency after six consecutive reuses was 92.10%; 91.30%; 89.8%, 87.90%; 83.3 and 78.1%. This indicates that the 12.0Bi_2S_3/ZC was good stability and recyclability. Besides, the concentration of Zn and Co ion leaching was found 0.148 and 0.06 mg L^{-1} in the solution after six cycles. The results suggest that the utilization of Bi_2S_3 nanoparticles as a support material improves the durability of $ZnCo_2O_4$ catalysts. The amount of total organic carbon (COD) in the initial solution, start and end of light irradiation were fixed at pH 6.0, using 12.0Bi_2S_3/ZC with a catalyst/IC solution ratio of

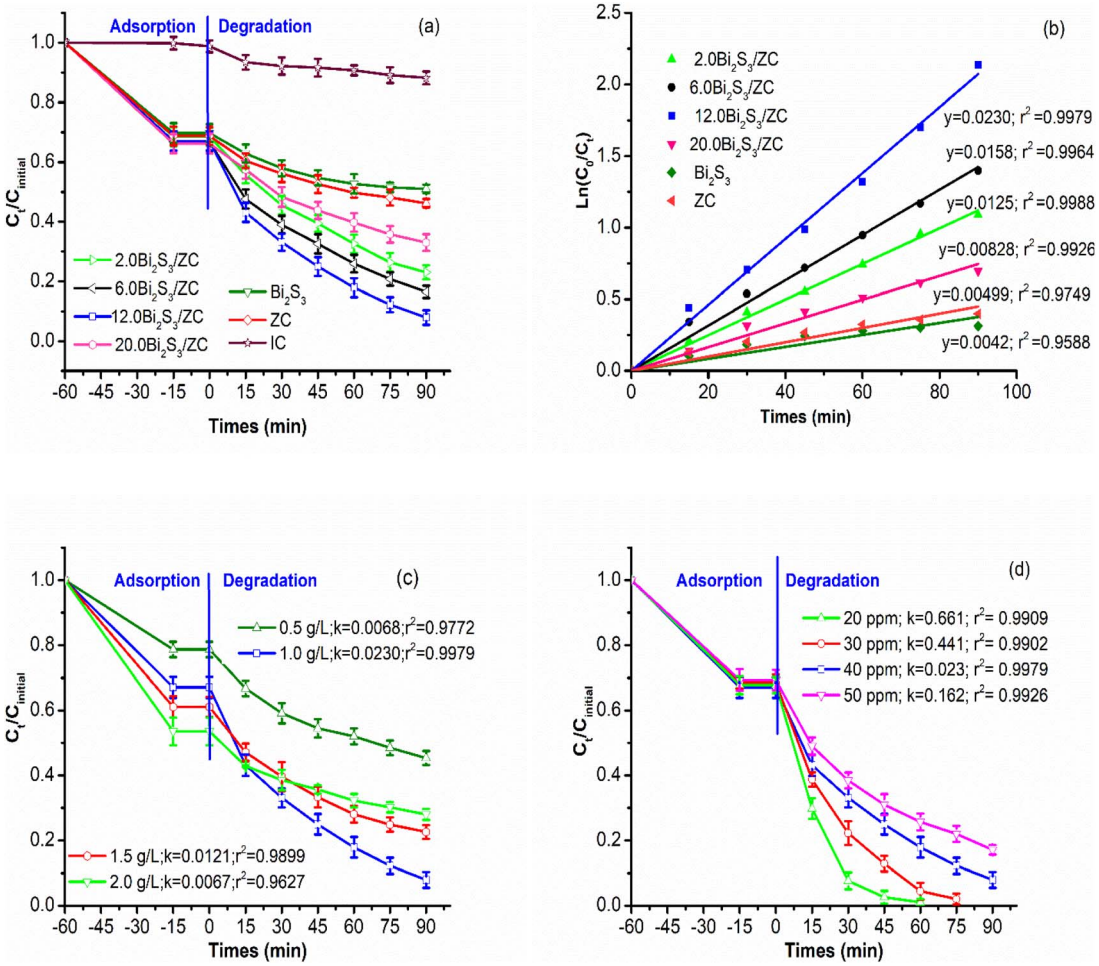

Fig. 8 (a and b) Effect of percentage of Bi_2S_3 in Bi_2S_3/ZC heterojunction (the mass percentage of $Bi_2S_3/ZnCo_2O_4$ = 2.0, 12.0, 16.0, 20.0, loading of $Bi_2S_3/ZnCo_2O_4$ = 1.0 g L^{-1}, pH 6, $C_{initial}$ = 40 ppm); (c) effect of the loading of 12.0Bi_2S_3/ZC (0.5–2.0 g L^{-1} of 12.0Bi_2S_3/ZC, pH 6, $C_{initial}$ = 40 ppm); (d) effect of initial IC concentration ($C_{initial}$ = 20–50 ppm, pH 6, loading of 12.0$Bi_2S_3/ZnCo_2O_4$ = 1.0 g L^{-1}); effect of the loading of 12.0Bi_2S_3/ZC.

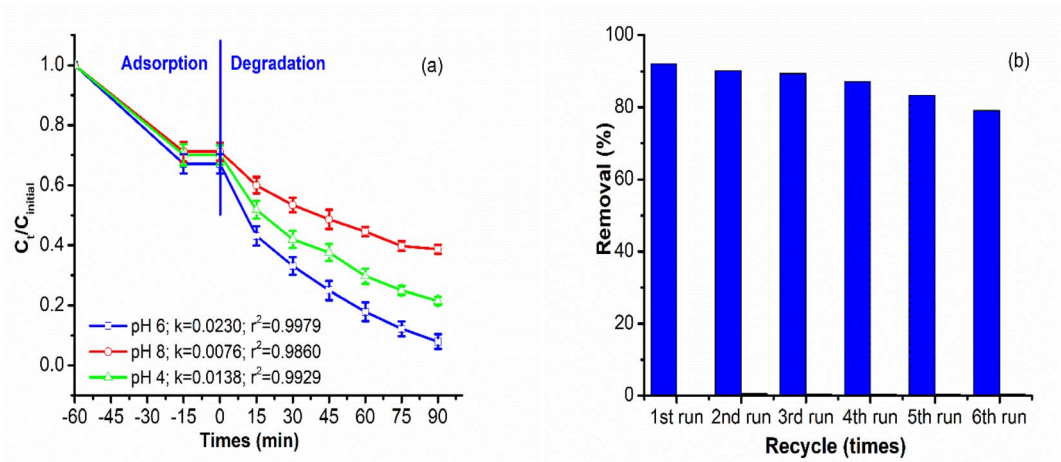

Fig. 9 (a) Effect of Initial pH value (pH 4–8, loading of 12.0$Bi_2S_3/ZnCo_2O_4$ = 1.0 g L^{-1}, $C_{initial}$ = 40 ppm); (b) stability and reusability.

1.0 g L^{-1}, were approximated to be about 74.256; 66.766 mg L^{-1} and 17.358 respectively. The COD removal efficiencies were achieved at about 10.1%; 86.05% start and end of 90 min visible light irradiation time. IC was completely mineralized to CO_2 and H_2O by photocatalytic degradation.

3.3.5 Effects of different scavengers. The main active species related to 12.0Bi_2S_3/ZC photocatalytic degradation of IC was studied Scavengers were used as ethanol 0.5 M, disodiumethylene diaminetetraacetate (Na_2EDTA) 0.01 M, and *p*-benzoquinone 0.025 mM, were used as $^{\bullet}OH$, h^+ and $^{\bullet}O_2^-$, respectively. As evident from Fig. 10, the degradation performance decreased in the order: of no quencher > ethanol > Na_2EDTA > *p*-benzoquinone. As observed, only approximately 55% (with $k = 0.0046\ min^{-1}$) and 50% (with $k = 0.0056\ min^{-1}$) of the IC were degraded when *p*-benzoquinone and Na_2EDTA were added to the system. The experiments indicated that the generated $^{\bullet}O_2^-$ radicals and h^+ were the dominant active species than $OH^{\bullet}$ radicals in the photocatalytic degradation of IC.

3.3.6 Possible photocatalytic mechanism. The diagram in Fig. 11 illustrates the suggested photocatalytic mechanism of the 12.0Bi_2S_3/ZC photocatalyst heterojunction. Before contact, p-type ZC has a Fermi level lower than those for n-type Bi_2S_3, so, electron directional diffusion from the Fermi level of n-type Bi_2S_3 to the Fermi level p-type ZC due to different Fermi levels. On another side, the hole diffused from VB of ZC to VB of Bi_2S_3 at the interface junction area. As a result, a depletion area was formed between the interface of ZC and Bi_2S_3 which accumulated negative charges on the ZC side and positive charges in Bi_2S_3. The Fermi level of Bi_2S_3 shifted downward while the Fermi level of ZC upward, to attain the equilibration. As mentioned above, a flat band potential of the $Bi_2S_3/ZnCo_2O_4$ heterostructure photocatalyst has shifted positively.

n-Bi_2S_3 nanoparticles warped on the ZC nanosheet formed a significant amount of interfacial sites, allowing for easy migration of the photoinduced charge carriers through the junction from one side to another. After contact, the Fermi level between p-ZC and n-Bi_2S_3 was equal, 12.0Bi_2S_3/ZC heterojunction generated electrons and holes pair at both CB and VB of ZC and Bi_2S_3 under light illumination. The movement of photogenerated electrons from the CB of $ZnCo_2O_4$ to the CB of Bi_2S_3 is facilitated. This result agrees with XPS, Co2p peak of 12.0Bi_2S_3/ZC shift to higher binding compared to ZC due to electron cloud density in ZC decrease. In particular, the internal electric field region is formed at the interface of the junction, which is accelerated and separated whole photoexcited electron–hole charge pairs, and that restricted the possibility of a photogenerated charge carrier recombining. This transfer leads to an increase in richer electrons in the CB of Bi_2S_3. The CB electrons of Bi_2S_3 are capable of reacting with O_2 absorbed on the surface, resulting in the production of the one-electron reduction of dioxygen O_2 such as superoxide radical anion ($^{\bullet}O_2^-$). This is because CB Bi_2S_3 has a greater negative potential than $O_2/^{\bullet}O_2^-$ (−0.33 V *vs.* NHE),[46,47] as follows;

$$\text{CB of } Bi_2S_3\ (e^-) + O_2 \rightarrow {}^{\bullet}O_2^-$$

$$^{\bullet}O_2^- + \text{IC} \rightarrow \text{degradation products}$$

In addition, the holes of Bi_2S_3 migrate towards the VB of $ZnCo_2O_4$ with the helpful support of a built-in electric field for can directly decompose IC.[25,43] The decoloration of IC can also be contributed by the remaining holes (h^+) at the VB of Bi_2S_3.[30,33]

The reasons why Bi_2S_3/ZC heterostructure shows excellent photocatalyst performance are as follows: (i) the Bi_2S composited with $ZnCo_2O_4$ improved photon absorption; (ii) an n–p heterojunction constructs inner built-in potential at the interface between Bi_2S_3 and ZC. Consequently, an increased quantity of free charges accumulates at the junction, as proven by the M-S tests; (iii) the HRTEM image demonstrates that the Bi_2S_3 amorphous layer, which is deposited onto the $ZnCo_2O_4$ structure, functions as a catalyst that enables charge injection, thus generating more photogenerated pathways. This is a critical factor in enhancing the activity of the photocatalyst. Therefore, the heterostructure formed between Bi_2S_3 and ZC exhibits

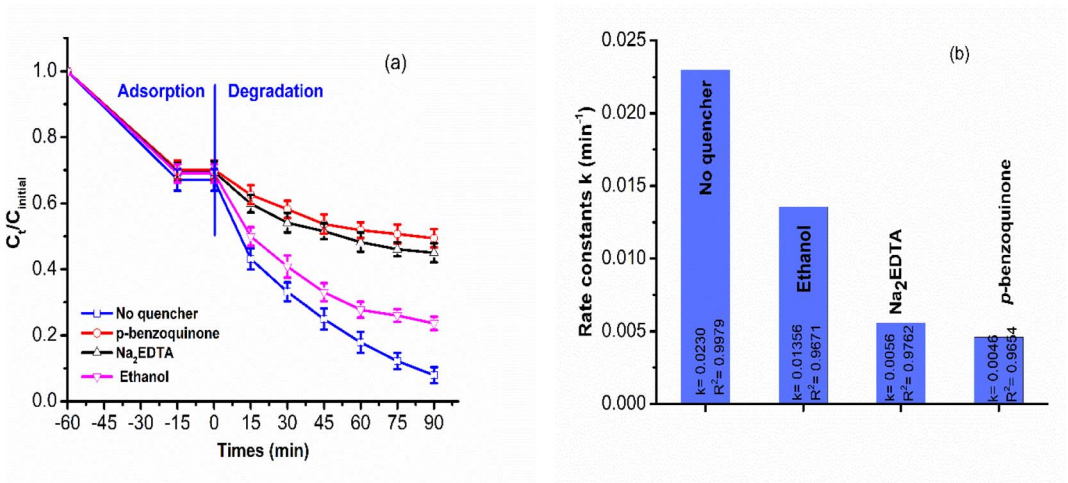

Fig. 10 (a and b) Effects of different scavengers on indigo carmine degradation over 12.0Bi_2S_3/ZC.

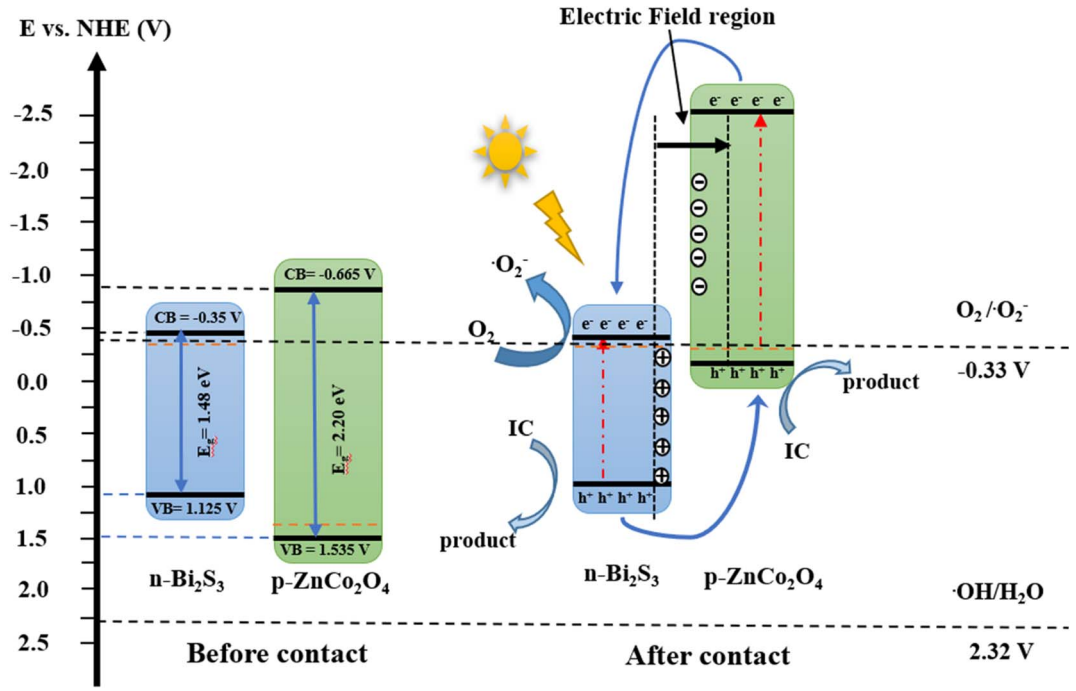

Fig. 11 Possible photocatalytic mechanism.

potential as a photocatalyst for the decomposition of diverse water pollutants in the presence of natural sunlight.

4. Conclusion

In summary, p–n heterojunction $x.0Bi_2S_3$/ZC ($x = 1, 2, 6, 12, 20$) photocatalysts were successful. The chemical structure, morphology, optical, and photoelectrical properties of $x.0Bi_2S_3$/ZC powder were analyzed. By controlling the molar amounts of Na_2S and $BiNO_3$, we have found that the Bi_2S_3 modification can tremendously boost the photocatalytic performance of ZC. When compared to pure ZC, the self-biased photocurrent density of $12.0Bi_2S_3$/ZC is 7.3 times higher. The EIS results offer enhanced comprehension of the function participated by Bi_2S_3 in the efficient separation and transfer of photogenerated charge carriers due to the contribution of an internal electric field. The results find that the $12.0Bi_2S_3$/ZC showed a higher efficiency of photodegradation than that of ZC and Bi_2S_3 for the degradation of IC and the degradation rate is 5 times higher than that of ZC. A pseudo-first-order kinetics equation is perfectly suitable for the IC decomposition of an $x.0Bi_2S_3$/ZC catalyst. Additionally, the results of different scavengers indicated that the important active species for IC decomposition were $O_2^{\bullet -}$ and h^+.

Author contributions

Nguyen Thi Mai Tho: methodology, writing – original draft, validation, writing – review & editing, project administration. Nguyen Van Cuong: investigation, resources. Luu Thi Viet Ha: data curation, software. Nguyen Quoc Thang: investigation, resources. Dang Huu Phuc: writing – review & editing.

Conflicts of interest

The authors declare that they have no known competing interests that could have appeared to influence the work reported in this paper.

Acknowledgements

This work is supported by Industrial University of Ho Chi Minh City (IUH), Ho Chi Minh, Vietnam under grant number 22/1HH01.

References

1 S. Wang, T. He, J. Yun, Y. Hu, M. Xiao, A. Du and L. Wang, *Adv. Funct. Mater.*, 2018, **28**, 1802685.
2 S. Lodha, A. Jain and P. B. Punjabi, *Arabian J. Chem.*, 2011, **4**, 383–387.
3 M. N. Chong, B. Jin, C. W. K. Chow and C. Saint, *Water Res.*, 2010, **44**, 2997–3027.
4 S. Ammar, R. Abdelhedi, C. Flox, C. Arias and E. Brillas, *Environ. Chem. Lett.*, 2006, **4**, 229–233.
5 A. Hernández-Gordillo, V. Rodríguez-González, S. Oros-Ruiz and R. Gómez, *Catal. Today*, 2016, **266**, 27–35.
6 M. Cheng, G. Zeng, D. Huang, C. Lai, P. Xu, C. Zhang and Y. Liu, *Chem. Eng. J.*, 2016, **284**, 582–598.
7 Md. T. Uddin, M. Z. Bin Mukhlish and Md. R. H. Patwary, *Desalin. Water Treat.*, 2021, **212**, 311–322.
8 K. Maeda, K. Ishimaki, Y. Tokunaga, D. Lu and M. Eguchi, *Angew. Chem., Int. Ed.*, 2016, **55**, 8309–8313.
9 M. Shao, Y. Shao, S. Ding, R. Tong, X. Zhong, L. Yao, W. F. Ip, B. Xu, X.-Q. Shi, Y.-Y. Sun, X. Wang and H. Pan, *ACS Sustainable Chem. Eng.*, 2019, **7**, 4220–4229.

10 S. S. Wong, M. J. Hülsey, H. An and N. Yan, *Catal. Sci. Technol.*, 2022, **12**, 5217–5228.
11 S. Song, J. Qu, P. Han, M. J. Hülsey, G. Zhang, Y. Wang, S. Wang, D. Chen, J. Lu and N. Yan, *Nat. Commun.*, 2020, **11**, 4899.
12 D. R. Kumar, S. Kesavan, M. L. Baynosa, V. Q. Nguyen and J.-J. Shim, *J. Colloid Interface Sci.*, 2018, **530**, 361–371.
13 W. Dai, J. Yu, S. Luo, X. Hu, L. Yang, S. Zhang, B. Li, X. Luo and J. Zou, *Chem. Eng. J.*, 2020, **389**, 123430.
14 K. Ai, Y. Liu, J. Liu, Q. Yuan, Y. He and L. Lu, *Adv. Mater.*, 2011, **23**, 4886–4891.
15 M. Y. Malca, H. Bao, T. Bastaille, N. K. Saadé, J. M. Kinsella, T. Friščić and A. Moores, *Chem. Mater.*, 2017, **29**, 7766–7773.
16 B. Shao, X. Liu, Z. Liu, G. Zeng, Q. Liang, C. Liang, Y. Cheng, W. Zhang, Y. Liu and S. Gong, *Chem. Eng. J.*, 2019, **368**, 730–745.
17 A. Pandikumar, K. Jothivenkatachalam and S. Moscow, *Heterojunction Photocatalytic Materials*, Jenny Stanford Publishing, New York, 2022.
18 A. Galán-González, A. K. Sivan, J. Hernández-Ferrer, L. Bowen, L. Di Mario, F. Martelli, A. M. Benito, W. K. Maser, M. U. Chaudhry, A. Gallant, D. A. Zeze and D. Atkinson, *ACS Appl. Nano Mater.*, 2020, **3**, 7781–7788.
19 Y. Liu, X. Yan, Z. Kang, Y. Li, Y. Shen, Y. Sun, L. Wang and Y. Zhang, *Sci. Rep.*, 2016, **6**, 29907.
20 J. Jian, R. Kumar and J. Sun, *ACS Appl. Energy Mater.*, 2020, **3**, 10408–10414.
21 K. Kim and J. H. Moon, *ACS Appl. Mater. Interfaces*, 2018, **10**, 34238–34244.
22 W. Zhang, C. Xu, E. Liu, J. Fan and X. Hu, *Appl. Surf. Sci.*, 2020, **515**, 146039.
23 X. Wang, P. Wu, Z. Zhao, L. Sun, Q. Deng, Z. Yin and X. Chen, *J. Mater. Sci.: Mater. Electron.*, 2020, **31**, 4895–4904.
24 J. Chen, J. Zhan, E. Lu, Y. Wan, Z. Jin and H. Qi, *Mater. Lett.*, 2018, **220**, 66–69.
25 J. Chen, J. Zhan, Y. Zhang and Y. Tang, *Chin. Chem. Lett.*, 2019, **30**, 735–738.
26 H. Benhebal, C. Wolfs, S. Kadi, R. G. Tilkin, B. Allouche, R. Belabid, V. Collard, A. Felten, P. Louette, S. D. Lambert and J. G. Mahy, *Inorganics*, 2019, **7**, 77.
27 L. Liu, G. Zhao, C. Li, S. Zhou, Y. Wang and F. Jiao, *Desalin. Water Treat.*, 2021, **217**, 411–421.
28 B. Tan, Y. Fang, Q. Chen, X. Ao and Y. Cao, *Opt. Mater.*, 2020, **109**, 110470.
29 S. Bera, S. Ghosh and R. N. Basu, *New J. Chem.*, 2018, **42**, 541–554.
30 S. Jiang, K. Zhou, Y. Shi, S. Lo, H. Xu, Y. Hu and Z. Gui, *Appl. Surf. Sci.*, 2014, **290**, 313–319.
31 I. Ahmad, M. S. Akhtar, E. Ahmed and M. Ahmad, *Sep. Purif. Technol.*, 2020, **245**, 116892.
32 X. Gao, G. Huang, H. Gao, C. Pan, H. Wang, J. Yan, Y. Liu, H. Qiu, N. Ma and J. Gao, *J. Alloys Compd.*, 2016, **674**, 98–108.
33 S. Sharma and N. Khare, *Colloid Polym. Sci.*, 2018, **296**, 1479–1489.
34 H. Han, H. Choi, S. Mhin, Y.-R. Hong, K. M. Kim, J. Kwon, G. Ali, K. Y. Chung, M. Je, H. N. Umh, D.-H. Lim, K. Davey, S.-Z. Qiao, U. Paik and T. Song, *Energy Environ. Sci.*, 2019, **12**, 2443–2454.
35 Y. Liu, Y. Zhang and L. Shi, *Colloids Surf., A*, 2022, **641**, 128577.
36 X. Li, L. Youji, X. Guo and Z. Jin, *Front. Chem. Sci. Eng.*, 2023, **17**, 606–616.
37 T. V. M. Sreekanth, R. Ramaraghavulu, S. V. Prabhakar Vattikuti, J. Shim and K. Yoo, *Mater. Lett.*, 2019, **253**, 450–453.
38 H. Song, J. Sun, T. Shen, L. Deng and X. Wang, *Catalysts*, 2021, **11**, 489.
39 Q.-Y. Tang, X.-L. Luo, S.-Y. Yang and Y.-H. Xu, *Sep. Purif. Technol.*, 2020, **248**, 117039.
40 X. Zhang, L. Shi and Y. Zhang, *J. Taiwan Inst. Chem. Eng.*, 2022, **132**, 104111.
41 T. Liu, L. Shi, Z. Wang and D. Liu, *Colloids Surf., A*, 2022, **632**, 127811.
42 X. Chang, T. Wang, P. Zhang, J. Zhang, A. Li and J. Gong, *J. Am. Chem. Soc.*, 2015, **137**, 8356–8359.
43 M. I. A. Abdel Maksoud, G. S. El-Sayyad, N. Mamdouh and W. M. A. El Rouby, *J. Inorg. Organomet. Polym. Mater.*, 2022, **32**, 3621–3639.
44 D. Zhang, S. Lv and Z. Luo, *RSC Adv.*, 2020, **10**, 1275–1280.
45 R. Abdel-Aziz, M. A. Ahmed and M. F. Abdel-Messih, *J. Photochem. Photobiol., A*, 2020, **389**, 112245.
46 F. Xu, Y. Yuan, H. Han, D. Wu, Z. Gao and K. Jiang, *CrystEngComm*, 2012, **14**, 3615.
47 V. S. Kirankumar and S. Sumathi, *Mater. Res. Bull.*, 2017, **93**, 74–82.